Fluid Dynamics & Materials Processing
DOI:10.32604/fdmp.2020.09681
Article

Shock-Wave/Rail-Fasteners Interaction for Two Rocket Sleds in the Supersonic Flow Regime

Bin Wang[1], Jing Zheng[1], Yuanyuan Yu[1,2], Runmin Lv[1] and Changyue Xu[1,*]

[1]Key Laboratory of Aircraft Environment Control and Life Support, MIIT, Nanjing University of Aeronautics and Astronautics, Nanjing, 210016, China
[2]AVIC Aerospace Life-Support Industries, Ltd., Xiangyang, 441003, China
[*]Corresponding Author: Changyue Xu. Email: cyxu@nuaa.edu.cn
Received: 15 January 2020; Accepted: 23 April 2020

Abstract: Rocket sleds belong to a category of large-scale test platforms running on the ground. The applications can be found in many fields, such as aerospace engineering, conventional weapons, and civil high-tech products. In the present work, shock-wave/rail-fasteners interaction is investigated numerically when the rocket sled is in supersonic flow conditions. Two typical rocket sled models are considered, i.e., an anti-D shaped version of the rocket sled and an axisymmetric slender-body variant. The dynamics for Mach number 2 have been simulated in the framework of a dynamic mesh method. The emerging shock waves can be categorized as head-shock, tailing-shock and reflected-shock. An unsteady large-scale vortex and related shock dynamics have been found for the anti-D shaped rocket sled. However, a quasi-steady flow state exists for the slender-body shaped rocket sled. It indicates that the axisymmetric geometry is more suitable for the effective production of rocket sleds. With the help of power spectral density analysis, we have also determined the characteristic frequencies related to shock-wave/rail-fasteners interaction. Furthermore, a harmonic phenomenon has been revealed, which is intimately related to a shock wave reflection mechanism.

Keywords: Rocket sled; shock wave; dynamic mesh method; ground effect

1 Introduction

Rocket sled belongs to a large-scale test platform running on the ground, which is mainly applied in many fields, such as aerospace engineering, conventional weapons, civil high-tech products, and so on [1–5]. Nowadays, the different rocket sleds have been built in many countries, such as USA, Britain, and China [6]. When the rocket sled moves at a high speed, such as supersonic regime, the potential damage may appear. Worst of all, the resonance may occur on the rocket sled. Thus, it attracts much attention on rocket sled vibration.

The main researches on rocket sleds in the literature are to investigate lift and drag forces of different rocket sleds [2,7–12]. For example, Zhang et al. [13] numerically investigated the aerodynamic characteristics of rocket sled in different conditions. Martin et al. [14] developed a system called rocket sled eXpert (RSX). In this system, the aerodynamic characteristics of several rocket sleds can be quickly

calculated. Xiao et al. [15] numerically predicted the ground effect on rocket sled tests, and an important basis for the reasonable arrangement of sensors was provided.

With the increasing requirements for high-speed experiments, the supersonic rocket sled was applied for ground tests. Unfortunately, a number of failures usually occurred due to rocket sled vibration. Two reasons relevant to rocket sled vibration were confirmed. One was the unstable thrust of rocket engines, and the other was the interaction between shock-wave and rail-fasteners. The variation originating from rocket thrust was irregular and difficult to predict. However, shock-wave oscillations were directly related to the operating speed [16]. From several failed launch tests, Lamb [16] revealed the periodic vibration phenomenon. It also provided the effective experimental data and theoretical support for vibration reduction design. Zhang et al. [17] established a virtual wind tunnel model using numerical simulation method. The aerodynamic characteristics of rocket sleds were also analyzed. They pointed out that the thrust eccentricity of rocket sleds was an important reason for serious vibration of rocket sleds. Zhang et al. [18] numerically investigated the aerodynamic performance for an 800 km/h evacuated tube train. They found that a slight shock wave appeared at the rear of tail car, which affected the aerodynamic force on the train. To our knowledge, the mechanisms relevant to shock-wave oscillations are sparse. Thus, in the present work, the shock-wave/rail-fasteners interaction and relevant mechanisms are investigated for two different rocket sleds.

A dynamic mesh approach is used to simulate dynamics for supersonic rocket sleds. The present paper is organized as follows. The numerical methods and physical models are briefly presented in Section 2. Results and discussion are presented in Section 3. Finally, the conclusions are given in Section 4.

2 Physical Models and Numerical Methods

2.1 Physical Models

Two rocket sleds are investigated in the present work. One is the anti-D shaped rocket sled which has a similar geometry in the subsonic rocket sled. The other is axisymmetric slender-body shaped rocket sled referring to some missile tests. To reduce the computational cost, it's necessary to reasonably simplify the physical models. The anti-D shaped rocket sled can be simplified to a two-dimensional (2D) body, and the slender body can be used to describe the three-dimensional (3D) axisymmetric rocket sled, as shown in Fig. 1. Furthermore, to investigate the interaction between the shock-wave and rail-fasteners, several square cylinders are set up on the ground with the same interval. For comparison, the height of 2D body is equal to the diameter of axisymmetric body D (D = 280 mm).

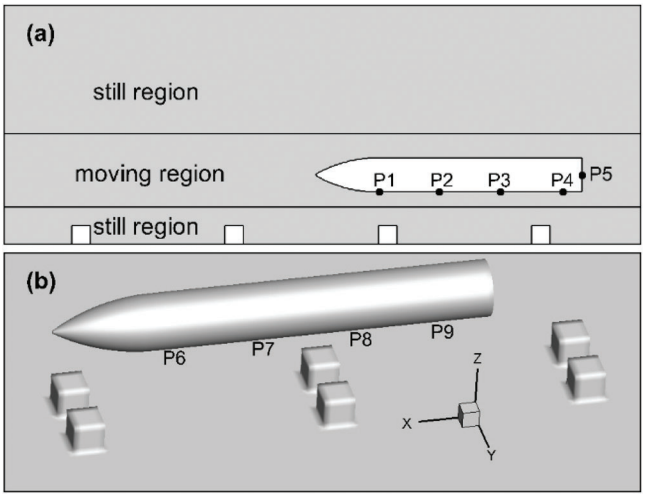

Figure 1: Two simplified rocket sled models: (a) 2D anti-D shaped rocket sled; (b) 3D slender-body shaped rocket sled

2.2 Numerical Methods

To simulate the supersonic motion of rocket sled, the 3D compressible Navier-Stokes equations are considered as governing equations. In the Cartesian coordinate system, the governing equations including mass, momentum and energy equations can be written as follows:

$$\frac{\partial \rho}{\partial t}+\frac{\partial u_i}{\partial x_i}=0, \tag{1}$$

$$\frac{\partial(\rho u_i)}{\partial t}+\frac{\partial(\rho u_i u_j)}{\partial x_j}=-\frac{\partial p}{\partial x_i}+\frac{\partial \tau_{ij}}{\partial x_j}, \tag{2}$$

$$\frac{\partial(\rho E)}{\partial t}+\frac{\partial[(\rho E+p)u_i]}{\partial x_i}=-\frac{\partial q_i}{\partial x_i}+\frac{\partial(u_j\tau_{ij})}{\partial x_i} \tag{3}$$

Here, ρ, u_i, p, E represent the density, velocity component, pressure and total energy, respectively. Based on the above analysis, two rocket sled models are investigated in the present work, i.e., 2D anti-D shaped rocket sled and 3D axisymmetric slender-body shaped rocket sled. To further reduce the computational cost, some approximate treatment can be performed. For the compressible flow at the higher Reynolds number, say about $O(10^7)$, the viscosity can be neglected. Thus, the Euler equations are used in the 3D case, i.e., $\tau_{ij}=0$.

The governing Eqs. (1)–(3) are solved by a finite volume method based on structured mesh, and the Fluent software is chosen. In this study, the density-based transient solver is used to solve the governing equations. For the density-based transient solver, the compressible governing equations including continuity, momentum, and energy are solved by means of time-marching solutions. To capture the discontinuity caused by shock waves, a second-order upwind scheme with Roe's flux difference splitting is introduced into two cases. For the 3D case, the inviscid flow is assumed. In the 2D case, the standard k-ε turbulent model proposed by Launder et al. [19] is used for turbulence closure, which can be written as,

$$\frac{\partial}{\partial t}(\rho k)+\frac{\partial}{\partial x_i}(\rho k u_i)=\frac{\partial}{\partial xj}\left[(\mu+\frac{\mu t}{\sigma k})\frac{\partial k}{\partial xj}\right]+Gk+Gb-\rho\varepsilon-YM+Sk, \tag{4}$$

$$\frac{\partial}{\partial t}(\rho \varepsilon)+\frac{\partial}{\partial x_i}(\rho \varepsilon u_i)=\frac{\partial}{\partial xj}\left[(\mu+\frac{\mu t}{\sigma \varepsilon})\frac{\partial \varepsilon}{\partial xj}\right]+C1\varepsilon\frac{\varepsilon}{k}(Gk+C3\varepsilon Gb)-C2\varepsilon\rho\frac{\varepsilon^2}{k}+S\varepsilon. \tag{5}$$

The initial values of k and ε are both 0 and their values on the boundary are also chosen as 0.

When the rocket sled runs along the rail at a supersonic speed, shock waves interact with rail-fastener due to the relative movement between rocket sled and rail-fasteners. To simulate this special flow, a dynamic mesh technique is acquired. Here, the dynamic mesh approach based on layering [20,21] is utilized. In the algorithm of dynamic mesh, the grid inside moving region is updated according to the change of boundary location. The solver will split or merge mesh based on the expansion or contraction of mesh region. When the grid spacing is larger than the upper limit, one layer will be divided into two layers. When the grid spacing is smaller than the lower limit, two layers will be merged into one layer. Two different regions need to be set up. One is the pre-specified motion achieved by a function involving the moving parameters. The other is a stationary region determined by the resolved flow field. We know that rocket sled runs along one fixed direction. Thus, the moving function can be described by setting a fixed Mach number.

In the 2D case, the initial condition is set as free-stream parameters. No-slip and adiabatic conditions are applied to the body and ground surface. The other boundaries are set as pressure far-field boundary

conditions. In 3D inviscid case, slip boundary condition is applied to body and ground surface, the other settings are the same as 2D case.

3 Results and Discussion

It is well known that two regions are required for the layering dynamic-mesh-method. The grid for 2D anti-D shaped rocket sled consists of 190,000 points in the moving region and 240,000 points in the stationary region. For the 3D slender-body shaped rocket sled, the grid points in the moving and stationary regions are 370000 and 1910000, respectively. To capture boundary layer for 2D anti-D shaped rocket sled, the first off-wall grid spacing is chosen as $1 \times 10^{-6}D$. Because the viscous effect is neglected for the supersonic flow past 3D body, the first off-wall grid spacing is $3.6 \times 10^{-3}D$. To guarantee the temporal accuracy, a sub-iteration technique is introduced with a fixed time step 3×10^{-6} second. At present, following the effective moving speed of supersonic rocket sled in China, the Mach number is chosen as 2. The Reynolds number is about 1.21×10^{7}. Here, the characteristic velocity is the running speed of rocket sled; the characteristic length is $D = 280$ mm; the values of density and viscosity coefficient are chosen at the static temperature 300 K.

Figs. 2 and 3 show the instantaneous flow patterns for two rocket sleds using the contours of static pressure. Here, the time interval is 0.0006 s, corresponding to a half period of sweeping two fasteners. For the convenience of discussion, a dimensionless pressure p/p_{∞} is analyzed with p_{∞} the environmental pressure. Because of the strong compressibility, shock waves appear in the flow fields of two rocket sleds, such as head-shock, trailing-shock, and reflected shock. In the flow field of anti-D shaped rocket sled, the obvious pressure-rise occurs behind the head-shock, according to the Rankine–Hugoniot conditions. When the head-shock sweeps over rail-fasteners, the high-pressure region also appears in the region between rocket sled and ground due to the shock-wave/rail-fasteners interaction. However, for the 3D axisymmetric rocket sled, the pressure-rise behind head-shock attenuates, which may be associated with the conical head-shock shrinking. Furthermore, the prominent flow stretching and distortion can be observed in the region between anti-D shaped rocket sled and ground. It means the eddy roll up easily appears under anti-D shaped rocket sled. While, it demonstrates a quasi-steady flow state under the 3D axisymmetric rocket sled, indicating that the axisymmetric geometry can improve the flow stability. In other words, the axisymmetric geometry is suitable for supersonic rocket sled.

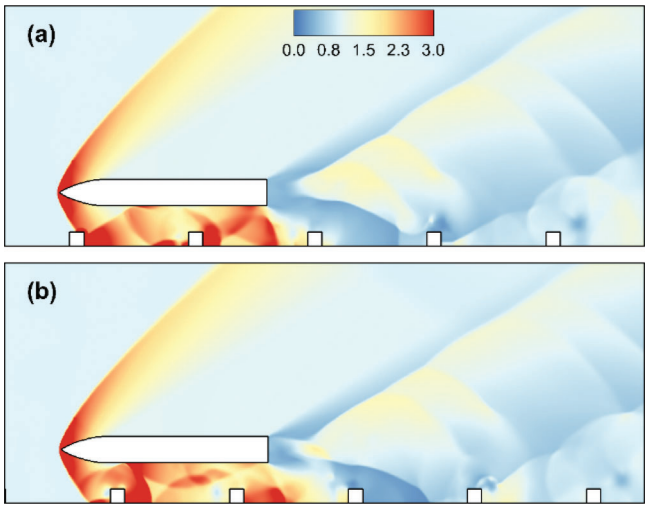

Figure 2: Instantaneous contours of static pressure for anti-D shaped rocket sled at two different times

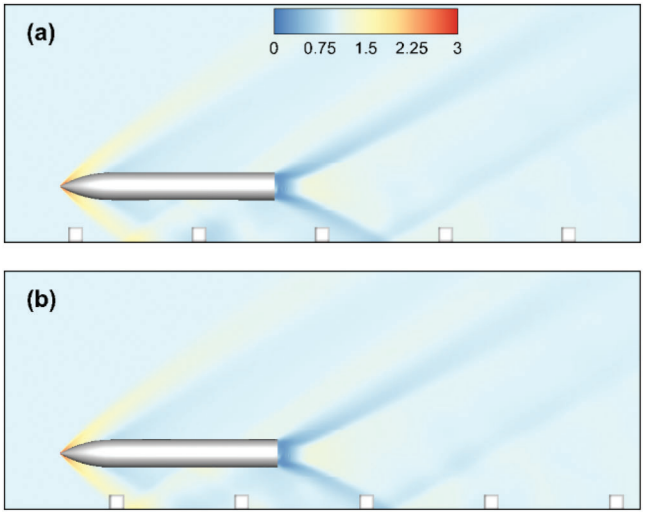

Figure 3: Instantaneous contours of static pressure for axisymmetric rocket sled at two different times

Figs. 4 and 5 show the density gradient along streamwise direction. The density gradient can obviously express the compression and expansion of air. It can be found that the reflected shock waves from head-shock can reflect back to the body, and the shock-wave/rail-fasteners interaction appear, consistent with the previous inference. The re-reflected shock waves also occur in the flow field of anti-D shaped rocket sled. Unlike anti-D shaped rocket sled, the reflected shock waves under axisymmetric rocket sled move upward and bypass the body. The intensity of reflected shock waves is obviously weakened, resulting in disappearance of re-reflected shock waves. Further, in the wake of anti-D shaped rocket sled, the obvious pressure waves can be observed, which may be the result of trailing-shock and rail-fasteners interaction.

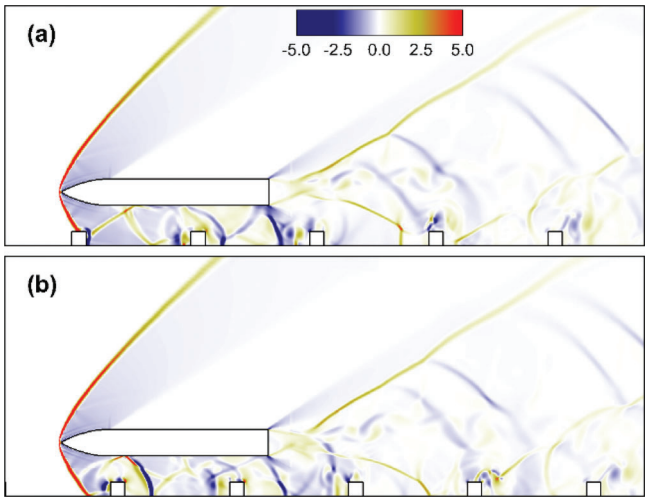

Figure 4: Density gradient along streamwise direction of anti-D shaped rocket sled at two different times

The description of flow field using primary variables (such as pressure) may miss some flow details. Lamb vector divergence $\nabla \cdot \boldsymbol{L}$ is closely related to the momentum and vorticity transport in the flow field [22,23]. Therefore, it is commonly used to understand the flow mechanisms. Here, Lamb vector is defined as $\boldsymbol{L} = \omega \times \boldsymbol{u}$. Hamman et al. [23] have given a physical interpretation for $\nabla \cdot \boldsymbol{L}$. The positive

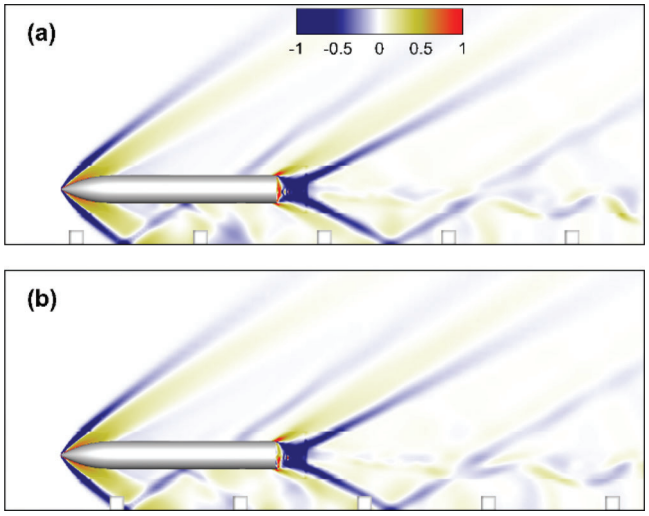

Figure 5: Density gradient along streamwise direction of axisymmetric rocket sled at two different times

value of $\nabla \cdot \boldsymbol{L}$ represents the flow stretching motion. While, the negative value of $\nabla \cdot \boldsymbol{L}$ denotes the vortical bearing motion. The alternating distributions of positive and negative values indicate the interaction between the strong strain region and vorticity region, which is associated with the momentum transport. Figs. 6 and 7 show the distributions of $\nabla \cdot \boldsymbol{L}$ at the symmetric planes of two rocket sleds. The obvious alternating structures can be found in the wake of two rocket sleds, associated with the moving body. In the flow field of anti-D shape rocket sled, the alternating structures can be observed near rail-fasteners due to shock-wave/rail-fasteners interaction. The alternating structures are also affected by the ground. At the initial stage of shock-wave/rail-fasteners interaction, the alternating structures are formed at leading edge of rail-fastener. As time goes on, the alternating structures move past rail-fasteners, resulting in eddy roll up behind rail-fasteners. Further, the alternating structures also appear behind head-shock, corresponding to shock oscillations. It indicates that the shock wave at the head of anti-D shaped rocket sled is more unstable than that in the flow field of axisymmetric rocket sled. In the wake of axisymmetric rocket sled, the positive value of $\nabla \cdot \boldsymbol{L}$ is wrapped by the negative value, as shown in Fig. 7. It means that the wake behind axisymmetric rocket sled is more stable.

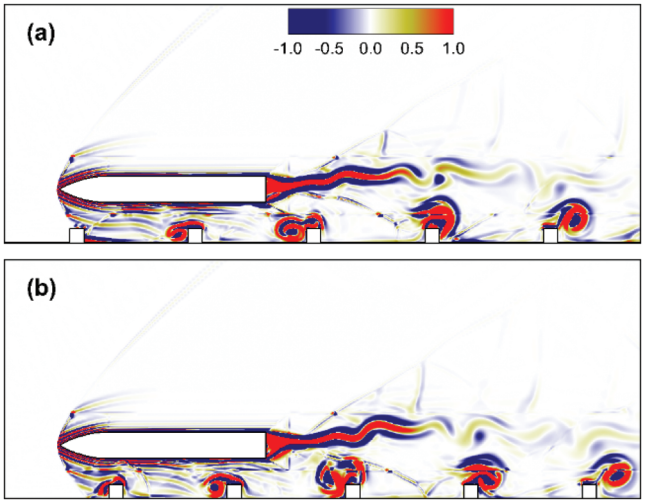

Figure 6: Contours of Lamb vector divergence for anti-D shaped rocket sled at two different times

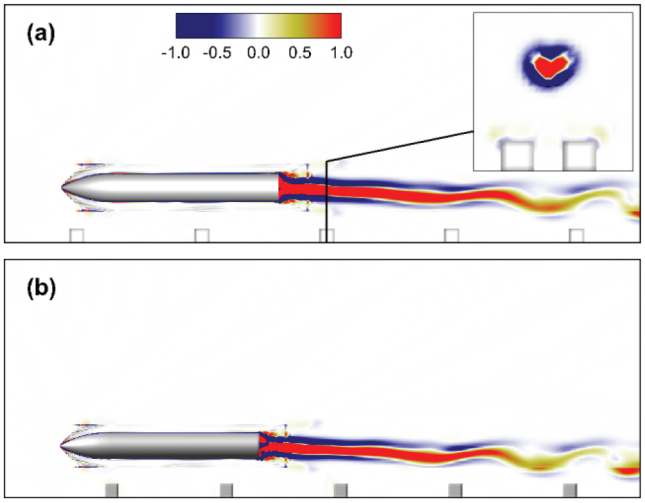

Figure 7: Contours of Lamb vector divergence for axisymmetric rocket sled at two different times

To analyze the flow fluctuations induced by the shock-wave/rail-fasteners interaction, the pressure signals near the wall are monitored using several pressure probes, as shown in Fig. 1. Firstly, we have a discussion for time histories of pressure signals at P1-P5, as shown in Fig. 8. The pressure probes P1-P4 are located below the body with the same intervals from $x = 0$ to $x = 1.5$ m. P5 is set on the base of anti-D shaped rocket sled. Because probe P1 is very close to the head of anti-D shaped rocket sled, the reflected shock waves only have a minor effect on the pressure signal at probe P1. Thus, the amplitude of pressure fluctuation at probe P1 is about 1 atm. P2 and P3 are directly affected by the reflected shock waves originating from the shock-wave/rail-fasteners interaction, so the pressure peak is higher, reaching approximately 5 atm. At P4, the amplitude reduces referred to the reflected shock waves attenuating. The pressure fluctuations at P5 are suppressed, which is closely associated with the dead air region in the near wake behind anti-D shaped rocket sled. Then, time histories of pressure signals at P6-P9 are analyzed, as exhibited in Fig. 9. Because the pressure fluctuations in dead air region are very weak, it cannot reveal the frequencies associated with shock-wave/rail-fasteners. Thus, the pressure probe isn't suggested to set in the dead air region. Similar to anti-D shaped rocket sled, the pressure fluctuations near the head of

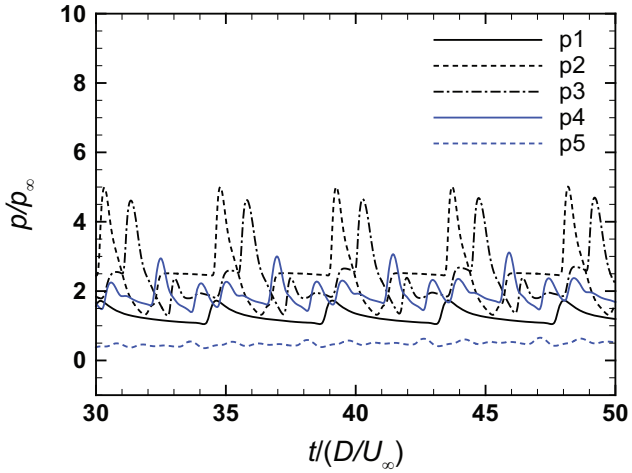

Figure 8: Time histories for pressure signals at probes P1–P5

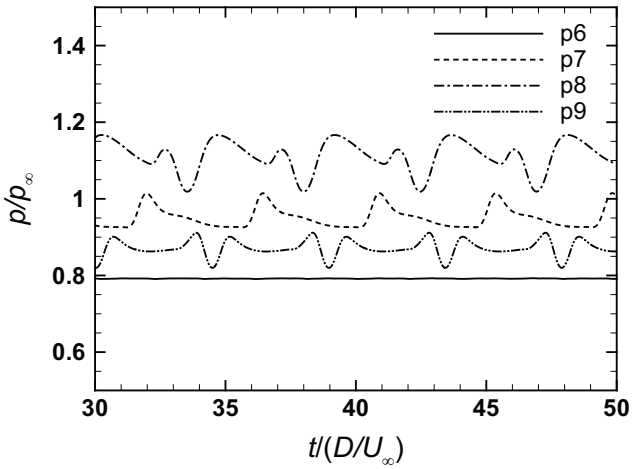

Figure 9: Time histories for pressure signals at probes P6–P9

axisymmetric rocket sled are also small. Furthermore, the amplitudes of pressure fluctuation at P7–P9 are smaller than that at P2–P4, which indicates that pressure fluctuations can be suppressed by axisymmetric rocket sled comparing with anti-D shaped rocket sled.

Usually, the characteristic frequency relevant to large-scale motion can be obtained using power spectral density (PSD) analysis [24]. Fig. 10 shows PSD curves for pressure signals at probes P2–P3. The highest peaks correspond to the characteristic frequencies, i.e., $f_1 \approx 0.571$ kHz, $f_2 \approx 1.048$ kHz and $f_3 \approx 1.619$ kHz. Here, f_1 is the dominated frequency referring to the shock-wave/rail-fasteners interaction. The approximate relationships can be obtained, i.e., $f_2 \approx 2f_1$ and $f_3 \approx 3f_1$. It implies that the harmonic phenomenon exists in the flow field of anti-D shaped rocket sled, which is consistent with the findings of Lamb [16]. The PSD analysis is also performed for pressure signals at probes P7–P9, as shown in Fig. 11. The characteristic frequencies corresponding to the first three peaks are $f_1 \approx 0.540$ kHz, $f_2 \approx 1.081$ kHz and $f_3 \approx 1.621$ kHz, respectively. The characteristic frequency f_1 is in good agreement with the experimental results of Lamb [16], indicating that the reliable predictions are obtained in the present computation. Although the complex alternating structures disappear near rail-fasteners, the similar relationships (i.e., $f_2 \approx 2f_1$ and $f_3 \approx 3f_1$) are also obtained. In the shear layer, the harmonic or

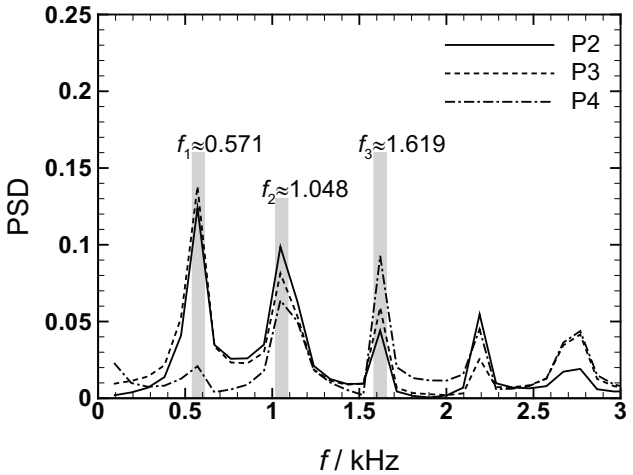

Figure 10: PSD profiles for pressure signals at probes P2–P4

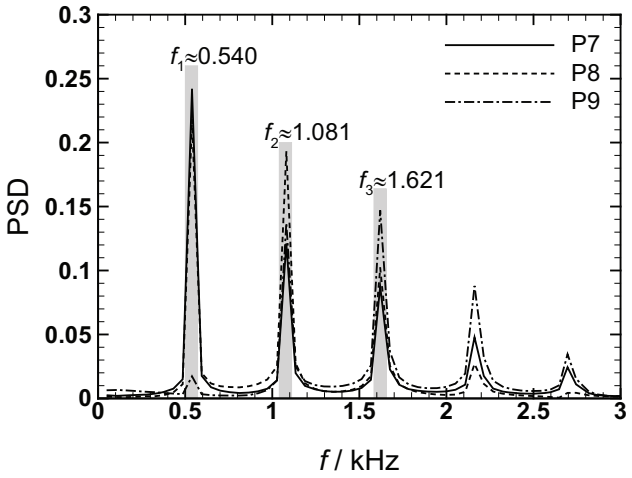

Figure 11: PSD profiles for pressure signals at probes P7–P9

subharmonic phenomenon can be also found, which is related to the vortex merging [25,26]. It means that the present harmonic phenomenon doesn't originate from the merging of vortices. It may be associated with shock reflecting induced by the shock-wave/rail-fasteners interaction.

4 Conclusions

In the present work, the dynamics for two supersonic rocket sleds along the rail have been studied using a dynamic mesh method. Based on the analysis and discussion for calculated results, some conclusions can be obtained as follows:

1) The dynamic grid method can be applied for simulating the movement of rocket sled. Different flow characteristics are observed for two different rocket sleds. In the flow field of anti-D shaped rocket sled, the unsteady large-scale vortex and shock motions appear due to the strong momentum transfer. However, a quasi-steady flow state exists in the flow field of axisymmetric rocket sled. It means the axisymmetric geometry is suitable for the rocket sled.

2) Based on the power spectral density analysis, the characteristic frequencies of the shock-wave/rail-fasteners interaction are obtained. The harmonic phenomenon related to reflected shock waves has been revealed. Different from the harmonic phenomenon in the shear layer reduced by vortex merging, the present harmonic phenomenon is reasonably associated with the shock waves reflecting.

Funding Statement: This work was supported by the National Natural Science Foundation of China (Grant Nos. 11572154 and 11202100), Aeronautical Science Foundation of China (Grant No. 2017ZD10002) and the Priority Academic Program Development of Jiangsu Higher Education Institutions.

Conflicts of Interest: We declare that we have no conflicts of interest to this work. We also declare that we do not have any commercial or associative interest that represents a conflict of interest in connection with this work.

References

1. Meacham, M. B., Gallon, J. C., Johnson, M. R., Natzic, D. B., Thompson, N. (2015). Rocket sled strength testing of large, supersonic parachute. *Daytona Beach, FL, AIAA Paper 2015-2163.*
2. Rigali, D. J., Feltz, L. V. (1968). High speed monorail rocket sleds for aerodynamic testing at high Reynolds numbers. *Journal of Spacecraft, 5(11),* 1341–1346. DOI 10.2514/3.29480.
3. Mcspadden, H. J., Higgins, R. R. (2004). The history of hurricane mesa test facility. *Fort Lauderdale, Florida, AIAA Paper 2004-3336.*

4. Meacham, M. B., Kennett, A., Townsend, D. J. (2013). Rocket sled propelled testing of a supersonic inflatable aerodynamic decelerator. *Daytona Beach, Florida, AIAA Paper 2013-1351.*
5. Zhan, Z. S., Wen, T. Y. (1995). The development of the protective helmet and oxygen mask against the wind blast at a velocity of 1000 km/h. *Acta Aeronautica et Astronautical Sinica, 16(1),* 18–22.
6. Zhou, Z. X., Zhou, S. H. (1979). *Atlas of foreign rocket pulley*. Beijing: National Defense Industry Press.
7. Lofthouse, A., Hughson, M., Palazotto, A. (2002). Hypersonic test sled external flow field investigation using computational fluid dynamics. *Reno, Nevada, AIAA Paper 2002-0306.*
8. Lofthouse, A., Hughson, M., Palazotto, A. (2003). Computational aerodynamic analysis of the flow field about a hypervelocity test sled. *Reno, Nevada, AIAA Paper 2003-0981.*
9. Stewart, B. L., Neil, B. (2005). Non-vitiated hypersonic propulsion system testing at the Holloman high speed test track. *Tucson, Arizona, AIAA Paper 2005-3896.*
10. Dang, T. J., Liu, Z., Zhou, X. W., Sun, Y. C., Li, J. (2019). Numerical investigation on aerodynamic parameters of deflector of hypersonic rocket sled. *Journal of Solid Rocket Technology.* http://kns.cnki.net/kcms/detail/61.1176.V.20190920.1443.002.html.
11. Praharaj, S. C., Roger, R. P. (1996). Aerodynamic computations of integrated missile-on-sled vehicles. *Reno, Nevada, AIAA Paper 1996-290.*
12. Zou, W. H. (2008). *Numerical simulation of rocket sled aerodynamics (Ph.D. Thesis)*. Nanjing University of Science and Technology.
13. Zhang, C. X., Lyu, S. Y., Xie, B. T., Wang, B. L. (2018). Study on aerodynamic characteristics of the wing of winged rocket sled under strong ground effect environment. *Journal of Ordnance Equipment Engineering, 39 (09),* 89–92.
14. Martin, C. H., Michael, R. M., Stanley, C. P., Paul, M. S., Judy, A. F. (2006). Engineering analysis for rocket sled aerodynamic. *Reno, Nevada, AIAA Paper 2006-664.*
15. Xiao, H., Gao, C., Sun, L. (2011). Numerical simulation of ground effect in blunt body rocket skid-test. *Journal of Missile and Missile Guidance, 31(04),* 102–104.
16. Lamb, J. L. (2000). Critical velocities for rocket sled excitation of rail resonance. *Johns Hopkins APL Technical Digest, 21(3),* 448–458.
17. Zhang, L. Q., Deng, Z. C., Chen, X. D., Shi, J., Yan, J. (2011). Numerical simulation of aerodynamic characteristics of sledding supersonic monorail rocket. *Chinese Journal of Trajectory, 23(04),* 100–104.
18. Zhang, X., Jiang, Y., Li, T. (2020). Effect of streamlined nose length on the aerodynamic performance of an 800 km/h evacuated tube train. *Fluid Dynamics & Materials Processing, 16(1),* 67–76. DOI 10.32604/fdmp.2020.07776.
19. Launder, B. E., Spalding, D. B. (1972). *Lectures in mathematical models of turbulence*. London, England: Academic Press.
20. Fu, D. B., Jiang, Y. (2007). Simulation of jet flow during missile launching with dynamic mesh. *Journal of Astronautics, 28(02),* 423–426.
21. Mi, B. G., Zhan, H., Zhu, J. (2013). Simulation of aerodynamic drag of high-speed train in evacuated tube transportation. *Chinese Journal of Vacuum Science and Technology, 33(09),* 877–882.
22. Wu, J. Z., Lu, X. Y., Zhuang, L. X. (2007). Integral force acting on a body due to local flow structures. *Journal of Fluid Mechanics, 576,* 265–286. DOI 10.1017/S0022112006004551.
23. Hamman, C. W., Klewicki, J. C., Kirby, R. M. (2008). On the lamb vector divergence in Navier-stokes flows. *Journal of Fluid Mechanics, 610,* 261–284. DOI 10.1017/S0022112008002760.
24. Xi, Y. H. (2012). *Aerodynamic characteristics and operation safety of high-speed trains under transverse wind (Ph.D. Thesis)*. Beijing Jiaotong University.
25. Dong, Y. F., Wei, Z. L., Xu, C. (1997). Transition of separated shear layer from order to chaos. *Physics of Fluids, 9 (9),* 2580–2584. DOI 10.1063/1.869374.
26. Xu, C. Y., Zhang, Y. T., Hou, B., Sun, J. H. (2019). Numerical investigations of the compressible turbulent flow past wavy-axis cylinder. *Fluid Dynamics Research, 51(5),* 055502. DOI 10.1088/1873-7005/ab2f84.